doi:10.1038/nature12203

1.0 Net Characteristic Normalizations

For any vector field on a sphere $\mathbf{v}(\theta,\varphi)$, where θ is colatitude and φ is longitude (Fig. S1), we can compute several net characteristics of that field by integrating $\mathbf{v}$ over the surface of the sphere. The vector and tensor definitions of four net characteristics (net rotation, net dipole, net quadrupole, and net stretching) are defined in the Methods Summary in the main text, but their magnitudes are determined by the normalization chosen for each net characteristic function. Here we define normalization factors that yield net characteristic amplitudes that correspond to the maximum velocity of a representative velocity field for each net characteristic (Fig. S2).

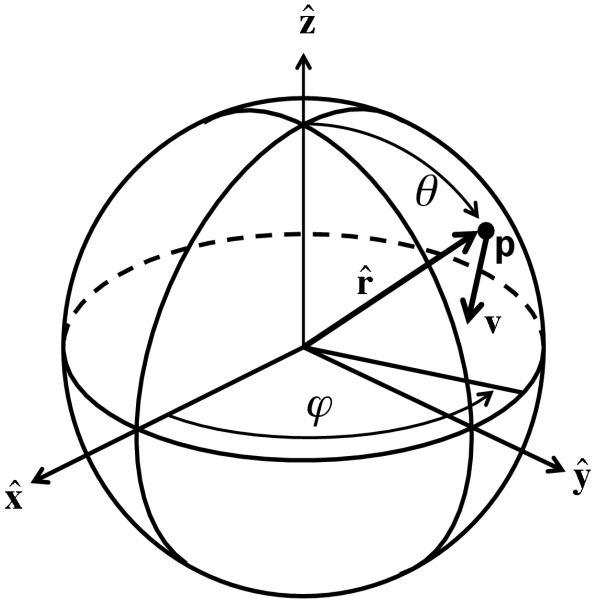

Figure S1. Spherical (θ, φ, *r*), and Cartesian (*x*, *y*, *z*) reference frames, and an arbitrary point **p** on the Earth's surface ($r = R_E$) moving with velocity $\mathbf{v}(\theta,\varphi)$.

1.1 Net Rotation

Solid body net rotation about the north pole (Fig. 1a) can be expressed as an eastward-oriented velocity field with amplitude that depends on θ as $v_\theta = 0$ and $v_\varphi = v_R \sin\theta$, where v_R is the maximum velocity amplitude occuring at $\theta = \pi/2$ (on the equator). This vector field is exemplified in Fig. S2a, where v_R=5 cm/yr. In Cartesian coordinates this velocity is expressed as $\mathbf{v} = \left(-v_R \sin\theta\sin\varphi, v_R \sin\theta\cos\varphi, 0\right)$. The net rotation vector **R** is calculated by crossing the local normal $\hat{\mathbf{r}} = \left(\sin\theta\cos\varphi, \sin\theta\sin\varphi, \cos\theta\right)$ with **v** and integrating, following the definition of **R** given by *Ricard et al.* [1991]:

$$\mathbf{R} = \frac{3}{2A_0}\int_{A_0} \hat{\mathbf{r}}\times\mathbf{v}\,dA = \frac{3v_R\hat{\mathbf{z}}}{2(4\pi)}\int_0^{2\pi}\int_0^{\pi}\sin^3\theta\,d\theta\,d\phi = v_R\hat{\mathbf{z}} \qquad \text{(S1)}$$

Thus, the magnitude of the net rotation vector, **R**, is equal to v_R, which is the net rotation velocity occurring along the net rotation equator (Fig. S2a).

Note that the net rotation vector **R** can also be obtained from the antisymmetric matrix **N** (defined in eq. 2). We can show this by writing (2) as:

$$\mathbf{L} = \frac{1}{A_0}\int_{A_0} \hat{\mathbf{r}}\otimes\mathbf{v}\,dA = \frac{1}{A_0}\int_{A_0}\begin{bmatrix} r_x v_x & r_x v_y & r_x v_z \\ r_y v_x & r_y v_y & r_y v_z \\ r_z v_x & r_z v_y & r_z v_z \end{bmatrix} dA \qquad \text{(S2)}$$

Then the symmetric (**M**) and antisymmetric (**N**) components of **L**=**M**+**N** are:

$$\mathbf{M} = \frac{1}{2A_0}\int_{A_0}\begin{bmatrix} 2r_x v_x & r_x v_y + r_y v_x & r_x v_z + r_z v_x \\ r_y v_x + r_x v_y & 2r_y v_y & r_y v_z + r_z v_y \\ r_z v_x + r_x v_z & r_z v_y + r_y v_z & 2r_z v_z \end{bmatrix} dA \quad \mathbf{N} = \frac{1}{2A_0}\int_{A_0}\begin{bmatrix} 0 & r_x v_y - r_y v_x & r_x v_z - r_z v_x \\ r_y v_x - r_x v_y & 0 & r_y v_z - r_z v_y \\ r_z v_x - r_x v_z & r_z v_y - r_y v_z & 0 \end{bmatrix} dA \qquad \text{(S3)}$$

Note that the cross product components of the net rotation vector **R** from (S1) can be re-

expressed in terms of the components of the anti-symmetric matrix **N**:

$$R_k = 3N_{ij}\varepsilon_{ijk}/2 \tag{S4}$$

where ε_{ijk} is the Levi-Civita permutation symbol. Thus, the components of the antisymmetric matrix **N** define the net rotation vector **R**.

1.2 Net Dipole

A pure dipole vector field with a (positive) convergence pole at the north pole (Fig. 1b) has the form $v_\theta = -\left(v_D \sin\theta\right)$ and $v_\varphi = 0$ (Fig. S2b), or $\mathbf{v} = -v_D \sin\theta\left(\cos\theta\cos\varphi, \cos\theta\sin\varphi, -\sin\theta\right)$ in Cartesian coordinates (Fig. S2b). Applying **v** to the definition of the net dipole in (1) gives:

$$\mathbf{D} = \frac{3}{2A_0}\int_{A_0}\mathbf{v}\,dA = \frac{3v_D\hat{\mathbf{z}}}{2(4\pi)}\int_0^{2\pi}\int_0^{\pi}\sin^3\theta\,d\theta\,d\phi = v_D\hat{\mathbf{z}} \tag{S5}$$

Thus, the magnitude of the dipole vector **D** is equal to v_D, which is the maximum poleward velocity, occurring along the dipole equator (Fig. S2b).

1.3 Net Quadrupole

We define the quadrupole velocity field, with positive (convergent), intermediate (null), and negative (divergent) poles (defined by the $\mathbf{m}_1$, $\mathbf{m}_2$, and $\mathbf{m}_3$ eigenvectors, respectively) coincident with **y**-, **z**-, and **x**-axes, respectively (Fig. 1c). In this case $v_\theta = 0$ and $v_\varphi = v_Q \sin\theta\sin 2\varphi$, or $\mathbf{v} = v_Q\left(-\sin\theta\sin 2\varphi\sin\varphi, \sin\theta\sin 2\varphi\cos\varphi, 0\right)$ in a Cartesian system (Fig. S2c). Integration of the outer product (S2) yields:

$$\mathbf{L} = \frac{v_Q}{A_0}\int_0^{2\pi}\int_0^{\pi}\begin{bmatrix}\sin\theta\cos\varphi\\ \sin\theta\sin\varphi\\ \cos\theta\end{bmatrix}\begin{bmatrix}-\sin\theta\sin\varphi\sin 2\varphi & \sin\theta\cos\varphi\sin 2\varphi & 0\end{bmatrix}\sin\theta\,d\theta\,d\varphi = \frac{v_Q}{6}\begin{bmatrix}-1 & 0 & 0\\ 0 & 1 & 0\\ 0 & 0 & 0\end{bmatrix} \tag{S6}$$

Solving for **Q** by diagonalizing **M** and applying (3) as described in the main text, we find:

$$\mathbf{Q} = \begin{bmatrix}v_Q & 0 & 0\\ 0 & 0 & 0\\ 0 & 0 & -v_Q\end{bmatrix} \tag{S7}$$

where the corresponding eigenvectors $\mathbf{m}_1$, $\mathbf{m}_2$, and $\mathbf{m}_3$ are parallel to the **y**, **z**, and **x** axes, respectively (Fig. 1c, S2c), producing divergence poles at (θ = π/2, φ = 0) and (π/2, π), convergent poles at (π/2, ±π/2) and intermediate poles at θ = 0 and θ = π. The quadrupole amplitude in (S7) is Q=v_Q, and thus is equal to that field's largest vector magnitude, which occurs midway between the convergent and divergent poles (Fig. S2c).

1.4 Net Stretching

We define the positive net stretching velocity field as convergent toward both the north and south poles, and divergent away from the equator (Fig. 1d). In this case $v_\theta = -v_S \sin 2\theta$ and $v_\varphi = 0$, which is $\mathbf{v} = -v_S \sin 2\theta\left(\cos\theta\cos\varphi, \cos\theta\sin\varphi, -\sin\theta\right)$ in a Cartesian system (Fig. S2d). Again rewriting the outer product using (S2) and integrating, we find:

$$\mathbf{L}=\frac{v_S}{A_0}\int_0^{2\pi}\int_0^{\pi}\sin 2\theta\begin{bmatrix}\sin\theta\cos\varphi\\ \sin\theta\sin\varphi\\ \cos\theta\end{bmatrix}\begin{bmatrix}-\cos\theta\cos\varphi & -\cos\theta\sin\varphi & \sin\theta\end{bmatrix}\sin\theta\,d\theta\,d\varphi=\frac{4v_S}{15}\begin{bmatrix}-1/2 & 0 & 0\\ 0 & -1/2 & 0\\ 0 & 0 & 1\end{bmatrix} \quad \text{(S8)}$$

Solving for **S** by diagonalizing **M** and applying (3) as described in the main text (assuming that net stretching occurs in the presence of a larger quadrupole field to associate net stretching with the intermediate $\mathbf{m}_2$ eigenvector, as discussed below), we find:

$$\mathbf{S}=\begin{bmatrix}-v_S/2 & 0 & 0\\ 0 & v_S & 0\\ 0 & 0 & -v_S/2\end{bmatrix} \quad \text{(S9)}$$

where the associated eigenvectors $\mathbf{m}_1$, $\mathbf{m}_2$, and $\mathbf{m}_3$ are parallel to the **y**, **z**, and **x** axes, respectively (Figs. 1d, S2d). The resulting net stretching expressed by (S9) yields convergence poles at the piercing points of $\pm\mathbf{m}_2$ ($\theta = 0$ and $\theta = \pi$), and divergence away from the equator ($\theta = \pi/2$). The net stretching magnitude is thus $S=v_S$, which is again the maximum velocity within the pure net stretching field (Fig. S2d), occurring at $\theta = \pi/4$ and $\theta = 3\pi/4$. If $S=v_S$ is negative, then the sense of motion is reversed to produce "net flattening" with diverging intermediate poles (at $\theta = 0$ and $\theta = \pi$) and convergence toward the equator.

2.0 Separating the Quadrupole and Net Stretching Components

Note that our method for separating $\mathbf{M}_D$ into quadrupole and net stretching components is not unique. We have chosen to align the positive and negative quadrupole vectors (+**Q** and –**Q**) with $\mathbf{m}_1$ and $\mathbf{m}_3$ (Fig. 1c), which correspond to the most positive and most negative eigenvalues of **M** (μ_1 and μ_3, respectively), and the net stretching vector (+**S**) with $\mathbf{m}_2$ (Fig. 1d), which is associated with the intermediate eigenvalue (μ_2). However, we could have alternatively associated net stretching with the largest (μ_1) or smallest (μ_3) eigenvalues, which would distribute the deformation between the quadrupole and net stretching differently. For example, associating net stretching (+**S**) with $\mathbf{m}_3$ and the quadrupole vectors (+**Q** and –**Q**) with $\mathbf{m}_1$ and $\mathbf{m}_2$ changes (3) to:

$$\mathbf{M}_D=\begin{bmatrix}\mu_1 & 0 & 0\\ 0 & \mu_2 & 0\\ 0 & 0 & \mu_3\end{bmatrix}=\frac{\mathbf{Q}}{6}+\frac{4\mathbf{S}}{15}=\frac{1}{6}\begin{bmatrix}Q & 0 & 0\\ 0 & -Q & 0\\ 0 & 0 & 0\end{bmatrix}+\frac{4}{15}\begin{bmatrix}-S/2 & 0 & 0\\ 0 & -S/2 & 0\\ 0 & 0 & S\end{bmatrix} \quad \text{(S10)}$$

where $Q=6\mu_1+3\mu_3$ and $S=15\mu_3/4$. Applying this alternative method for separation to a pure quadrupole field for which $\mu_1=v_Q/6$, $\mu_2=0$, and $\mu_3=-v_Q/6$ (see above), we find new amplitudes for the quadrupole and net stretching components (specifically, we find $Q=v_Q/2$ and $S=-5v_Q/8$), and different orientations of the net quadrupole and net stretching vectors compared to our original method. Both methods accurately express the deformation described by $\mathbf{M}_D$ and associated eigenvectors, but do so in different ways. Our method of aligning the intermediate eigenvector ($\mathbf{m}_2$) with net stretching associates the largest amplitude eigenvalues (and the associated $\mathbf{m}_1$ and $\mathbf{m}_3$ eigenvectors) with quadrupole motion. For global plate motions, quadrupole motion tends to dominate (Fig. S3), which makes our choice of separation method convenient. Regardless of the method, however, the second order net characteristics computed using (2) are uniquely described by the eigenvectors $\mathbf{m}_1$, $\mathbf{m}_2$, and $\mathbf{m}_3$, and their associated eigenvalues. Our method consistently aligns these eigenvectors with the positive quadrupole

(+**Q**), net stretching (+**S**), and negative quadrupole (-**Q**) poles, respectively, and thus fully and uniquely describes the second order net characteristics of plate tectonic motions.

3.0 Extension of the *Torsvik et al.* [2010] Reconstruction back to 250 Ma, and Comparison with other Reconstructions

Torsvik et al. [2010] reconstructed plate motions globally back to 150 Ma (Fig. S6a-o), but reconstructed continental areas (i.e. all plates except for those in the Pacific basin) back to 250 Ma. To extend *Torsvik et al.'s* [2010] model back to 250 Ma for all areas, we used the global reconstruction of *Seton et al.* [2012] to reconstruct the motion of plates in the Pacific basin for the 150-200 Ma time period (Fig. S6p-t) and extended these Pacific plate motions for the 200-250 Ma time period (Fig. S6u-y) using the data archive supplementing *Seton et al.* [2012]. Poles of rotation and plate boundaries for the 150-250 Myr time period are included here as supplemental files and can be added to those published by *Torsvik et al.* [2010] to produce a global reconstruction back to 250 Ma.

Due to the lack of hotspot tracks, absolute plate motions in the Pacific basin, and hence the contribution of this basin to the plate tectonic dipole, are rather unconstrained for the entire 150-250 Ma period. *Seton et al.* [2010] assume that the Pacific plate - then a small plate at a triple junction - was fixed. Before ~180 Ma, relative plate motions for the Pacific, and therefore their contribution to the plate tectonic quadrupole, are also rather unconstrained, as no ocean floor is preserved before this time. *Seton et al.* [2010] assume that spreading away from the Pacific basin triple junction had been ongoing before 180 Ma. Before 230 Ma, their model assumes that the Farallon plate was fixed to North America.

The main differences between the models of *Torsvik et al.* [2010] and *Seton et al.* [2012] are that (1) the former use independent Pacific and African hotspot reference frames, whereas the latter use a plate circuit linking both hemispheres after 83 Ma, and that (2) *Torsvik et al.* [2010] use a simplified model of Pacific plate motions prior to 83 Ma. Different from *Seton et al.* [2012], *Doubrovine et al.* [2012] determine an absolute reference frame that fits hotspot tracks globally after 83 Ma. However, because *Seton et al.* [2012] and *Doubrovine et al.* [2012] were otherwise constructed similarly, their dipole and quadrupole results also look similar (compare Figs. S4 and S5), apart from a small shift due to their slightly differing absolute reference frames. *van der Meer et al.* [2010] suggest a westward shift of the reference frame peaking at 18° at 150 Ma. Applying a corresponding shift to the dipole and quadrupole locations would move divergent quadrupoles closer to the LLSVP centers.

Similarities and differences between these models help to characterize model uncertainties and to assess which model features are robust. The main uncertainty of our analysis comes from the fact that an increasingly smaller fraction of the ocean floor is preserved for older time periods, which means that the plate configuration for an increasingly larger fraction of the Earth's surface must be "best guessed". This missing fraction is referred to as "world uncertainty" by *Torsvik et al.* [2010], and reaches 60 % at 150 Ma. Given this, it would be difficult, and probably also misleading, to state formal uncertainties of our dipole and quadrupole locations. However, comparison between results for the different models presented here (Figs. 3, S4, S5) indicates that the location and stability of both the dipole axis and the quadrupole divergence are robust. The models also agree that quadrupole convergence poles moved from more polar locations

earlier towards more equatorial locations since the late Cretaceous, but differ somewhat in the rate and path of motion prior to the mid-Cretaceous.

4.0 Additional Supplemental Files: Digital Plate Boundaries & Rotation Poles (150-250 Ma)

Two additional files provide the lat-long locations of (1) digitized plate boundaries and (2) plate rotation stage poles for each plate for each 10 Myr interval between 150 and 250 Ma. The format of these files is that same as that of similar files provided for 0-150 Ma by *Torsvik et al.* [2010]. Indeed these files extend *Torsvik et al.'s* [2010] model back to 250 Ma (Fig. S6).

5.0 References Cited in Supplementary Materials

Doubrovine, P. V., Steinberger, B., and Torsvik, T. H. Absolute plate motions in a reference frame defined by moving hot spots in the Pacific, Atlantic, and Indian oceans, *Journal of Geophysical Research* 117, B09101, doi:10.1029/2011jb009072 (2012).

Duncan, R. A., & Clague, D. A. Pacific plate motion recorded by linear volcanic chains, in *The Ocean Basins and Margins*, *vol. 7A*, *The Pacific Ocean*, ed. by A. E. A. Nairn et al., pp. 89–121, Plenum, New York, doi:10.1007/978-1-4613-2351-8_3, (1985).

Koppers, A. A. P., Morgan, J. P., Morgan, J. W., & Staudigel, H. Testing the fixed hot spot hypothesis using $^{40}Ar/^{39}Ar$ age progressions along seamount trails, *Earth and Planetary Science Letters* 185, 237–252, doi:10.1016/S0012-821X(00)00387-3 (2001).

Ricard, Y., Doglioni, C., & Sabadini, R. Differential rotation between lithosphere and mantle: A consequence of lateral mantle viscosity variations, *Journal of Geophysical Research* 96, 8407-8415, doi:10.1029/91jb00204 (1991).

Seton, M., Müller, R. D., Zahirovic, S., Gaina, C., Torsvik, T., Shephard, G., Talsma, A., Gurnis, M., Turner, M., Maus, S., & Chandler, M. Global continental and ocean basin reconstructions since 200 Ma, *Earth-Science Reviews* 113, 212-270, doi:10.1016/j.earscirev.2012.03.002 (2012).

Torsvik, T. H., Steinberger, B., Gurnis, M., & Gaina, C. Plate tectonics and net lithosphere rotation over the past 150 My, *Earth & Planetary Sci. Lett.* 291, 106-112, doi:10.1016/j.epsl.2009.12.055 (2010).

van der Meer, D. G., Spakman, W., van Hinsbergen, D. J. J., Amaru, M. L., & Torsvik, T. H., Towards absolute plate motions constrained by lower-mantle slab remnants, *Nature Geoscience* 3, 36-40, doi:10.1038/ngeo708 (2010).

Wessel, P., & Kroenke, L. Pacific absolute plate motion since 145 Ma: An assessment of the fixed hot spot hypothesis, *Journal of Geophysical Research* 113, B06101, doi:10.1029/2007JB005499 (2008).

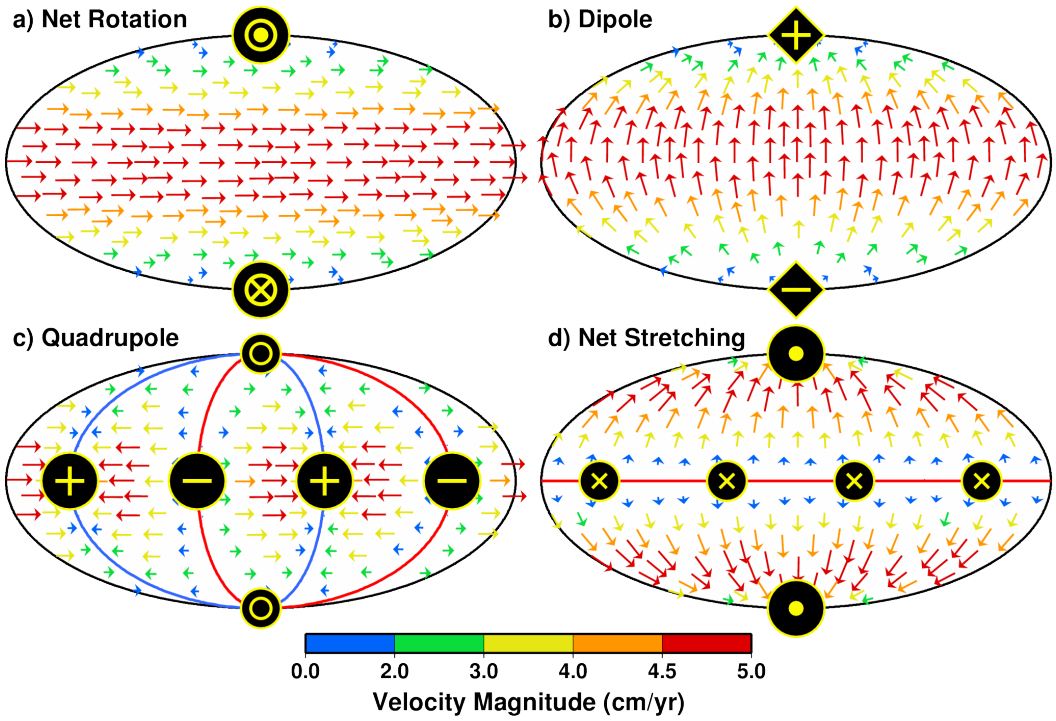

Figure S2. Representative velocity fields for (a) net rotation, (b) net dipole, (c) net quadrupole, and (d) net stretching, with functional forms as described in the text. Velocity direction is shown by arrows, and their length and color correspond to velocity magnitude. The maximum velocity magnitude in each case is 5 cm/yr, which also corresponds to the net characteristic magnitude for each case. The locations of net characteristic poles are denoted by symbols consistent with those defined in Fig. 1.

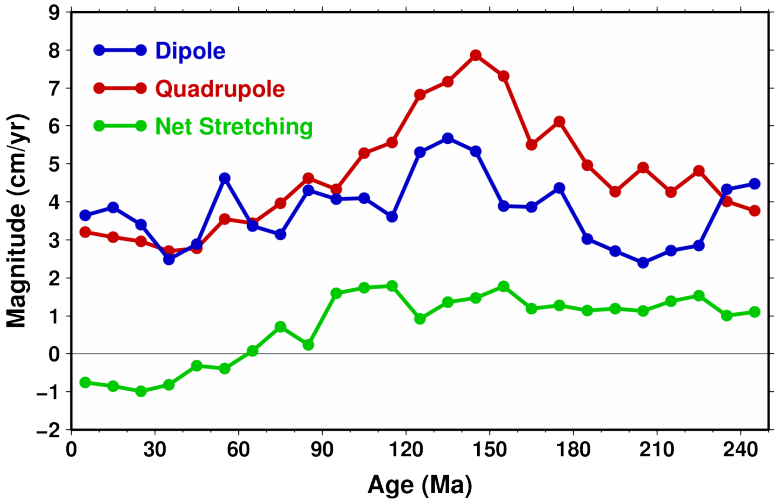

Figure S3. Magnitude of three net characteristic components (net dipole, net quadrupole, and net stretching as blue, red, and green lines) as a function of tectonic reconstruction age (Figs. 3, S6).

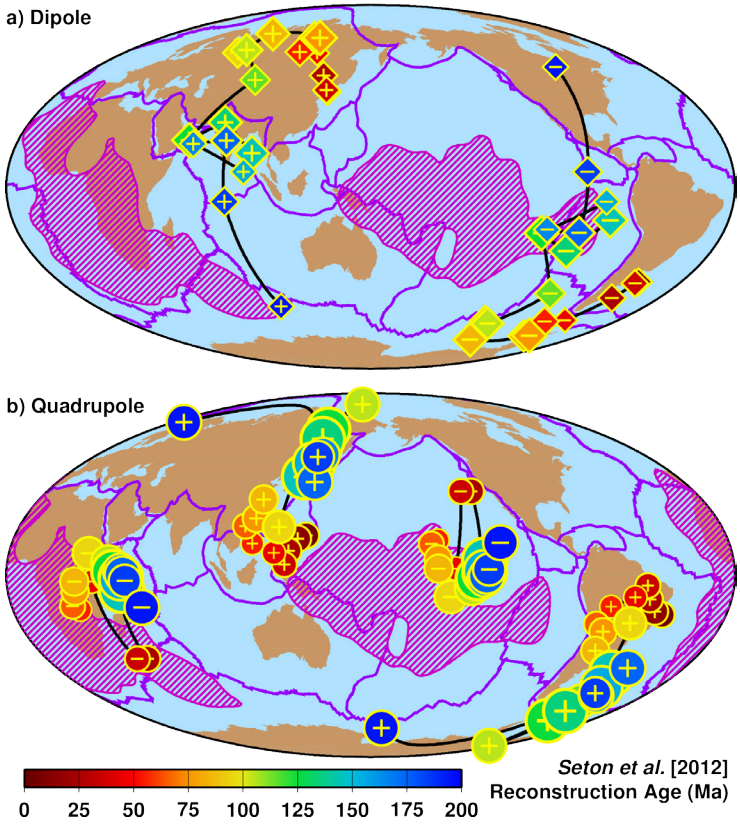

Figure S4. Motion of (a) dipole and (b) quadrupole net characteristic poles as a function of reconstruction age (similar to Fig. 3), but computed for the reconstruction of *Seton et al.* [2012], which extends back to 200 Myr.

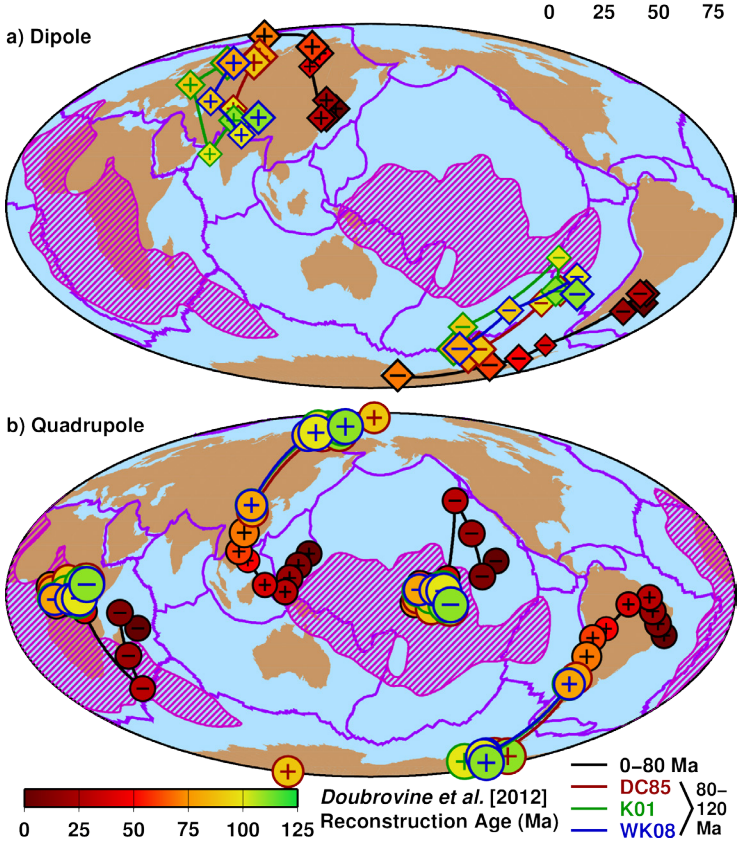

Figure S5. Motion of (a) dipole and (b) quadrupole net characteristic poles as a function of reconstruction age (similar to Fig. S4), but computed for the reconstruction of *Doubrovine et al.* [2012], which extends to 120 Ma. *Doubrovine et al.* [2012] presents three models for the 80-120 Ma timeframe, based on *Duncan & Clague* [1985], *Koppers et al.* [2001], and *Wessel & Kroenke* [2008] (which we denote as DC85, K01, and WK08, respectively). Here these three models can be distinguished by the color of the symbol boundary (red, green, and blue for DC85, K01, and WK08, respectively) for symbols in the 80-120 Ma timeframe. Black symbol outlines are used for the 0-80 Ma timeframe, for which *Doubrovine et al.* [2012] presents only one model.

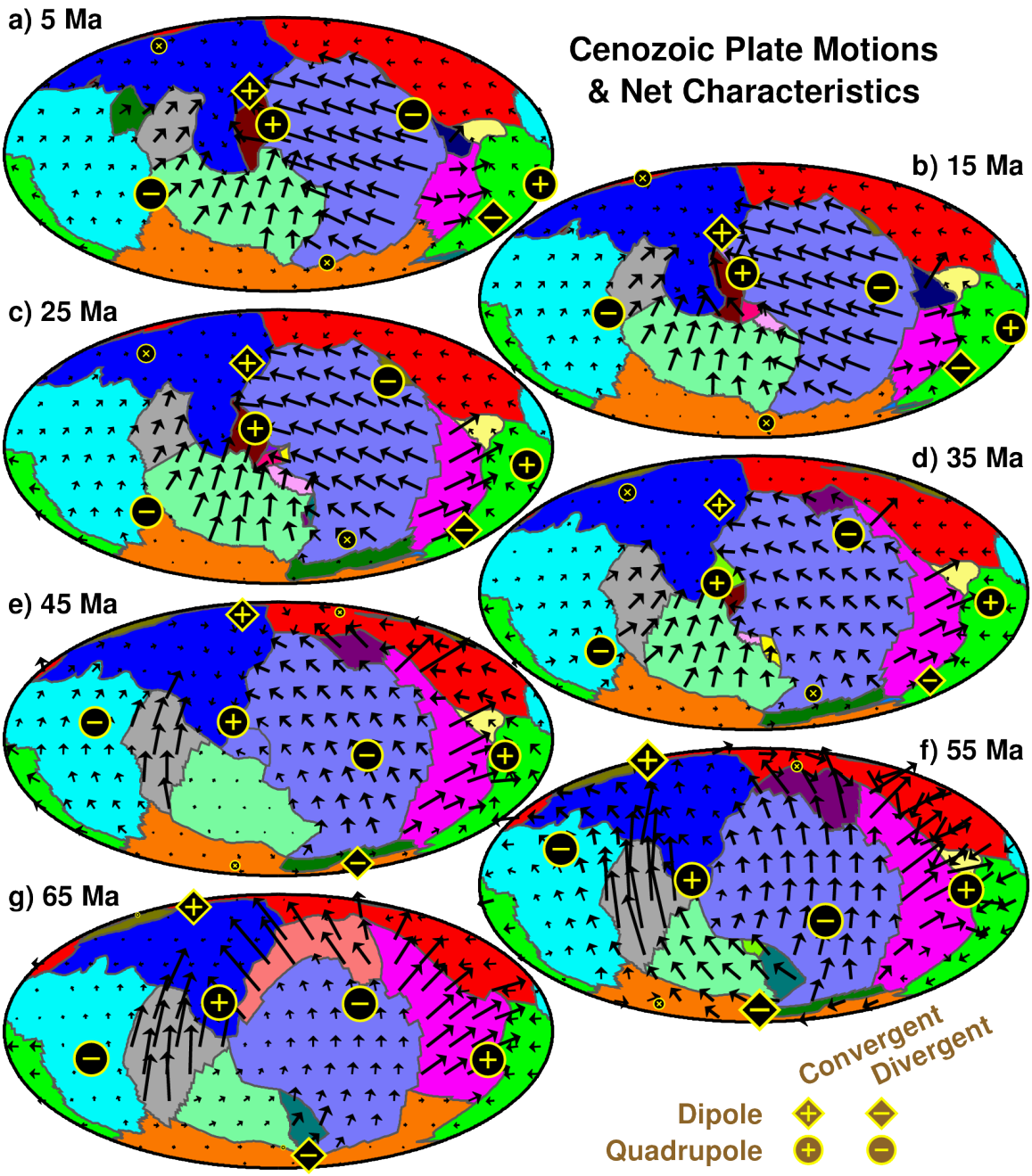

Figure S6. Plate motions (arrows) and computed net characteristic poles (symbols) for the Cenozoic (a-g), Cretaceous (h-o), Jurassic (p-t), and Triassic (u-y) time periods, based on the tectonic reconstruction of *Torsvik et al.* [2010] for the past 150 Ma, and extended back to 250 Ma by reconstructing the Pacific basin following *Seton et al.* [2012]. Reconstructions are in 10 Myr intervals (labeled age denotes middle of interval) over which plate motions are averaged.

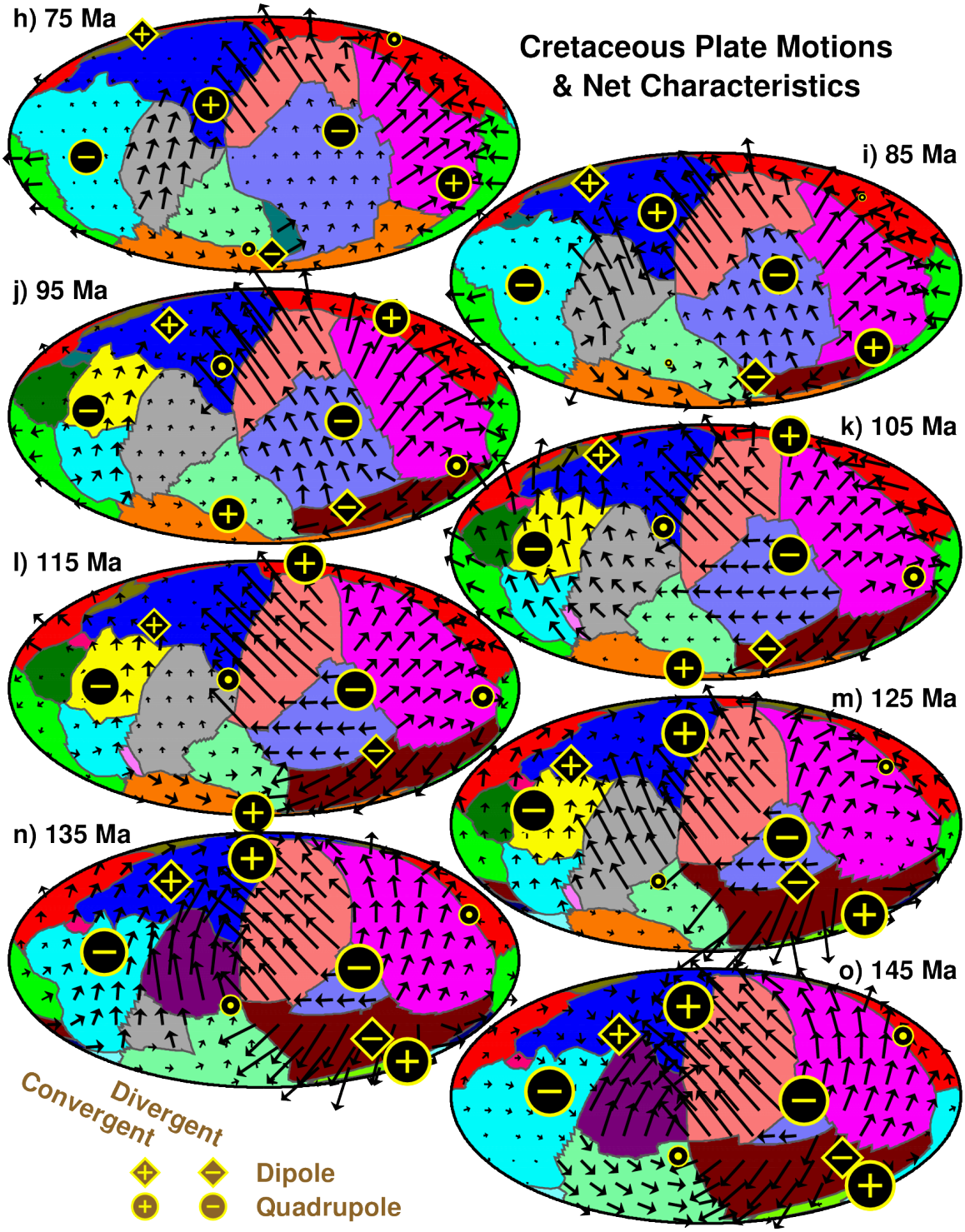

Figure S6. (continued, shown here for the Cretaceous)

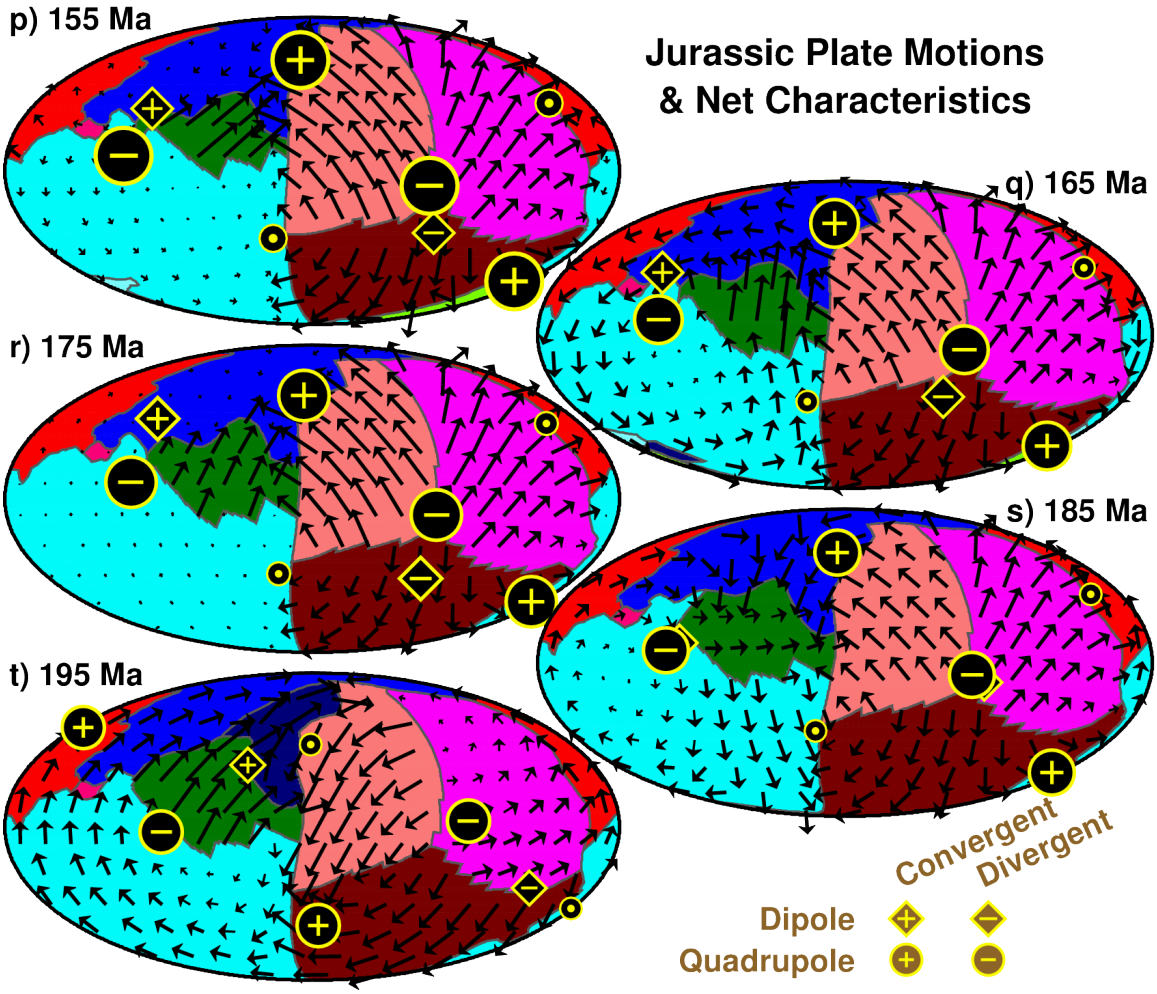

Figure S6. (continued, shown here for the Jurassic)

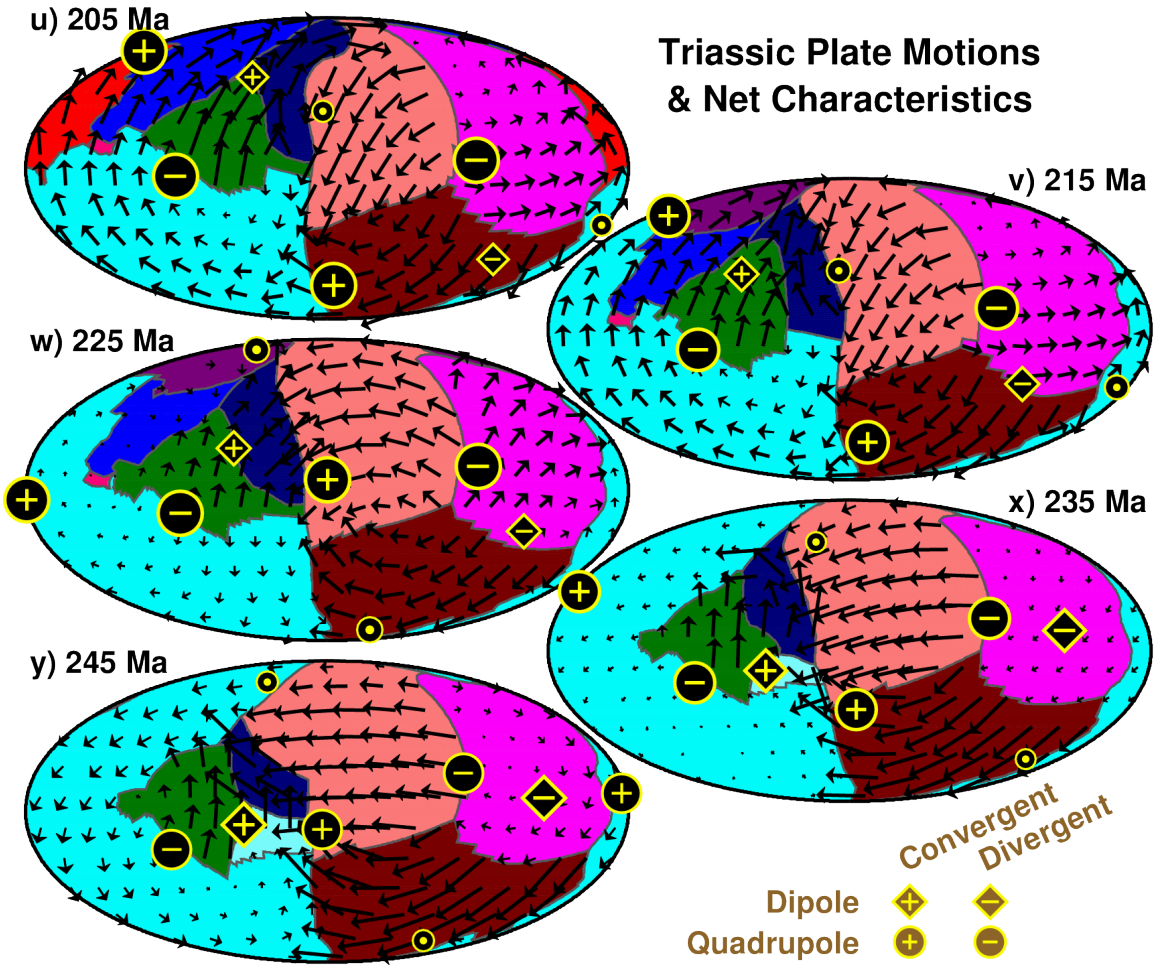

Figure S6. (continued, shown here for the Triassic)